# On Electrochemical Model-Based State Estimation for Lithium–Sulfur Batteries

Zhijia Huang<sup>®</sup>, Luis D. Couto<sup>®</sup>, Chitra Dangwal<sup>®</sup>, Shujie Xiao<sup>®</sup>, Wei Lv<sup>®</sup>, Dong Zhang<sup>®</sup>, and Scott J. Moura<sup>®</sup>, *Member*, *IEEE* 

Abstract—The high theoretical specific energy density of lithium-sulfur (Li-S) batteries positions them as an advanced next-generation battery system to overcome the limitations of conventional Li-ion batteries. Accurate estimation of the mass evolution of active sulfur species in Li-S cells is required, not only to monitor degradation mechanisms inside the cell but also to enable safe and efficient operation. The state estimation problem for electrochemical models (EMs) of Li-S cells is challenging, mainly due to the complex dynamics during discharge/charge processes. In this work, we consider a three-step 0-D EM with the "shuttle effect" for state estimation. The model's state observability is analyzed and the parameters are identified using experimental data. An extended Kalman filter is directly applied to the nonlinear differential-algebraic equation (DAE) system to estimate the differential and algebraic states from the measurements of voltage and current only. The simulation and experimental results demonstrate the effectiveness of the proposed observer design.

Index Terms—Kalman filter, lithium-sulfur (Li-S) battery, observability, state estimation.

## I. INTRODUCTION

URRENT lithium-ion battery (LIB) technology, unfortunately, does not meet the energy density requirements for fully electrifying long-haul trucks, aircraft, and other massor volume-sensitive applications. Therefore, developing new battery technologies beyond the horizon of Li-ion chemistries is significant for applications in high energy density storage systems [1]. Lithium-sulfur (Li-S) batteries have attracted attention today due to their high theoretical energy density

Manuscript received 14 June 2023; accepted 7 November 2023. Date of publication 7 December 2023; date of current version 25 April 2024. Recommended by Associate Editor A. Vahidi. (Zhijia Huang, Luis D. Couto, and Chitra Dangwal are co-first authors.) (Corresponding author: Dong Zhang.)

Thiiia Huang is with the Teinghua Berkeley Shenghen Institute

Zhijia Huang is with the Tsinghua-Berkeley Shenzhen Institute, Tsinghua Shenzhen International Graduate School, Tsinghua University, Shenzhen 518055, China (e-mail: hzj19@berkeley.edu).

Luis D. Couto is with Vlaamse Instelling voor Technologisch Onderzoek (VITO), Unit Energy Technology, B-2400 Mol, Belgium (e-mail: luis.coutomendonca@vito.be).

Chitra Dangwal and Scott J. Moura are with the Department of Civil and Environmental Engineering, University of California at Berkeley, Berkeley, CA 94720 USA (e-mail: chitra\_dangwal@berkeley.edu; smoura@berkeley.edu).

Shujie Xiao and Wei Lv are with the Shenzhen Geim Graphene Center, Tsinghua Shenzhen International Graduate School, Tsinghua University, Shenzhen 518055, China (e-mail: xsj92mrmuscle@163.com; lv.wei@sz.tsinghua.edu.cn).

Dong Zhang is with the School of Aerospace and Mechanical Engineering, The University of Oklahoma, Norman, OK 73019 USA (e-mail: dzhang@ou.edu).

Digital Object Identifier 10.1109/TCST.2023.3337589

(2500 Wh·kg<sup>-1</sup>), which results from the multielectron electrochemical redox reaction between lithium (Li) and sulfur. However, their practical use at a large scale is hindered by low sulfur utilization and poor cycling stability, which are attributed to the inferior electronic conductivity of sulfur, the diffusion and migration of soluble polysulfide intermediates ("shuttle effect"), and unstable Li metal anode [2]. To date, great efforts on cell design have been made to overcome these obstacles, including host material synthesis, electrolyte optimization, and lithium anode protection [3]. Besides, theoretical modeling and estimation techniques have also been explored in recent years, which not only helps gain important insights into the complex mechanisms for the rational design of better materials but also allows the cells to be controlled in a reliable and safe way in real applications [4]. For batteries that are used in electric vehicles (EVs), a battery management system (BMS) [5] is required to monitor the internal state of the battery, optimize usage, and prolong cycle life. Therefore, the development of an advanced BMS for Li-S batteries is urgently needed to estimate the internal electrochemical kinetics as well as internal states, i.e., estimation of the state of charge (SOC) and state of health (SOH).

Traditionally, estimation methods in LIBs rely on two key model features: 1) the relationship between open-circuit voltage (OCV) and SOC is a bijection [6] and 2) SOC is simply a scaled integral of electrical current [7]. These properties do not exist in Li-S batteries. First and foremost, the literature does not provide a precise mathematical definition of SOC with respect to the mass of sulfur species, to the authors' best knowledge. Second, the dynamics are characterized by a nonlinear differential-algebraic structure, which cannot be simply boiled down to the two aforementioned LIB model features. Finally, the voltage curve exhibits a wide flat region, which yields observability challenges, somewhat like lithium iron phosphate cells. In addition, the "shuttle effect" induces a self-discharge behavior where sulfur specifies will evolve without an externally applied current. Consequently, the Coulomb counting method cannot be used for accurate SOC estimation [8], [9].

Model-based estimation methods have been explored for accurate online state estimation. Equivalent circuit models (ECMs) [10], [11] and electrochemical models (EMs) [12], [13], [14] are the most studied models for LIBs in literature. ECMs have become the main battery model for online state estimation in EVs because of their relatively simple structure and low computational complexity. The main

1063-6536 © 2023 IEEE. Personal use is permitted, but republication/redistribution requires IEEE permission. See https://www.ieee.org/publications/rights/index.html for more information.

structure of ECMs for Li–S batteries is almost identical to that of LIBs. The discharge/charge behavior with current- and temperature-dependent parameters can be well reproduced [15], [16], [17], [18]. Methods that combine ECMs with adaptive filters have been adopted for SOC estimation in Li–S cells [19]. However, the convergence property deteriorates with increasing initial condition errors and increasingly dynamic current profiles. Accordingly, some joint estimators of parameters and SOC were then developed to further enhance estimation accuracy and robustness [20]. Despite the computational efficiency of ECMs, the true electrochemical processes inside Li–S batteries cannot be accurately represented across a range of operating conditions in real-life applications.

EMs provide insight into the internal electrochemical kinetics and Li-ion transport behavior. In literature, the most studied EMs for LIB are the pseudo-2-D (P2D) model [21] and the single particle model (SPM) [12], [13], [22]. However, EM-based estimation methods typically require more sophisticated algorithm designs, due to the complicated partial differential equations and many involved parameters, which is still a key challenge in online applications. That issue becomes even worse for Li-S batteries. Various EMs have been developed to capture important physical phenomena inside the Li-S battery, such as reaction mechanisms, precipitation/dissolution processes, transport limitations, and shuttle effect [23], [24], [25], [26], [27]. Most of these models can represent the key features of the voltage profiles: the highand low-voltage plateaus and the voltage dip in the transition region, but even for 1-D models, the complicated reaction steps and involved sulfur species require a large number of parameters, making it less practical for real-time control and estimation. Recently, a simplified model—the 0-D model has shown its potential as an efficient tool for monitoring and control because of its relatively low-order structure [28]. Xu et al. [29] demonstrated parameter identification and sensitivity analysis for a set of 0-D models, based on the number of possible reaction pathways. The most significant parameters and the fitting performance of the model have been evaluated based on experimental data. The model with the best fitting performance was then implemented with a Unscented Kalman Filter (UKF) for online estimation of the mass evolution of sulfur species in the discharging process. The estimation problem was simplified by converting the differential-algebraic equations (DAEs) to ordinary differential equations (ODEs), which may not always be possible. Besides that, the shuttle effect was not considered in their model, which is a crucial feature of Li-S batteries that largely affects battery dynamic behavior.

For Li–S batteries, the battery capacity is highly dependent on the active sulfur species inside the cell, which means that the SOC and SOH are both determined by the mass evolution of various polysulfide species. Therefore, it is crucial to accurately estimate these sulfur species during the discharge process. However, estimation based on 0-D models suffers from several challenges. First, the complex DAEs result in a nonlinear relationship among the measurable signals, system states, and parameters. Second, as also mentioned in [29], the sensitivity of the output voltage with respect to the

system states vanishes in the low voltage plateau, making it weakly observable. Third, the definition of SOC in Li–S cells is challenging because of multiple reduction pathways associated with different reacting species. Finally, the analysis and estimator design tools for nonlinear DAEs still need to be further explored for battery estimation problems.

In our preliminary work [30], we have proposed a state estimation algorithm for a two-step 0-D model using voltage and current measurements only, which enables the monitoring of the sulfur species and the reaction kinetics accurately during the battery discharge process. However, the simplified one-step reaction in high plateau cannot accurately capture the slope of the discharge voltage in reality. To overcome these challenges, the main contributions that separate this work and our preliminary studies are given as follows.

- The model and estimation algorithm are rigorously validated through experimental data to verify the performance and robustness that reflects the real-world application scenarios.
- 2) The two-step 0-D model is extended by adding a third step—a reduction reaction in the high plateau to more accurately capture the voltage dynamics. In addition, the shuttle effect is included in this model, which is a nonnegligible phenomenon in Li–S cells.
- 3) The local observability is analyzed using DAE techniques without prior model reductions. We then employ an extended Kalman filter directly based on the DAE system to estimate the internal states, which is further validated using experimental data.
- 4) The calculation of SOC for Li-S cells is proposed for the first time using sulfur species to reflect the effects of shuttling—a significant improvement against the heuristic coulomb counting method.

The remainder of this article is structured as follows. Section II introduces the 0-D EM and the DAE system. Section III analyzes the local observability of the nonlinear DAE system. A parameter identification process with experimental data is presented in Section IV. Section V presents the proposed EKF algorithm for state estimation. Simulation and experimental results are provided in Section VI. Section VII concludes this work.

### II. LI-S BATTERY MODEL

The Li–S battery cell is mainly composed of a metallic Li anode, an elemental sulfur cathode, an organic electrolyte, and a separator, as presented in Fig. 1(a). During a typical discharge process, Li-ions are electrochemically stripped from the Li metal anode and move to the cathode via the electrolyte. Elemental sulfur  $S_8^0$  at the cathode side undergoes a series of complicated electrochemical and chemical reactions to form the final discharge product Li<sub>2</sub>S, involving the formation of intermediate lithium polysulfides (LiPSs). The corresponding reactions operate in reverse to convert solid Li<sub>2</sub>S to dissolved LiPSs and then to elemental  $S_8^0$  upon charging [31]. Fig. 1(b) shows the typical two-plateau discharge/charge voltage profile of Li–S batteries. The high plateau, at approximately 2.4 V, involves the reduction of sulfur to Li<sub>2</sub>S<sub>4</sub> via multiple higher order Li<sub>2</sub>S<sub>8</sub> ( $4 \le n \le 8$ ). Then, on the low plateau at

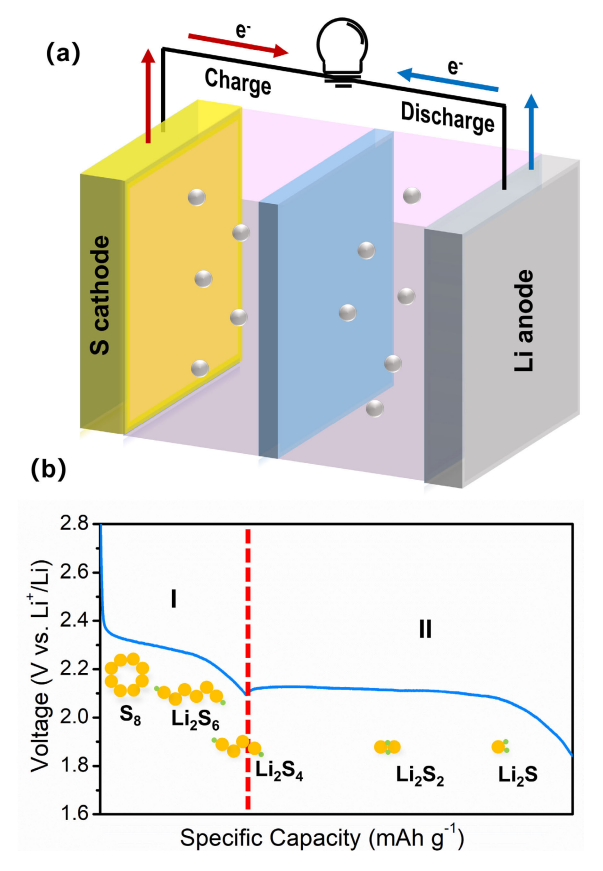


Fig. 1. (a) Li-S cell structure. (b) Galvanostatic discharge voltage profile and the involved polysulfides in I: high-voltage plateau and II: low-voltage plateau.

about 2.1 V, short-chain LiPSs are converted to solid  $\text{Li}_2\text{S}$ . During the discharge process, the intermediate LiPSs can easily dissolve into the organic electrolyte solution and then migrate between the cathode and anode, called the "shuttle effect," resulting in the loss of active material and low coulombic efficiency.

## A. Zero-Dimensional Model

A three-step 0-D model is used in this study, which follows the derivations in [28], [32], and [33]. Compared to the two-step model in our previous work [30], the time evolution of  $S_6^{2-}$  is considered in the high plateau. Fig. 2(a) shows the conversion process from the initial sulfur  $S_8$  into the final discharge product  $S_p$ , and the corresponding three-step electrochemical reaction chain is described as follows:

$$\frac{3}{8}S_8^0 + e^- \longleftrightarrow \frac{1}{2}S_6^{2-} \tag{1}$$

$$S_6^{2-} + e^- \longleftrightarrow \frac{3}{2} S_4^{2-}$$
 (2)

$$\frac{1}{6}S_4^{2-} + e^- \longleftrightarrow \frac{2}{3}S^{2-} \downarrow . \tag{3}$$

To simplify the model, this 0-D model only considers the sulfur evolution reactions on the cathode side, and the anode overpotential is neglected under the assumption of unlimited Li on the anode side [34]. As a 0-D model, the diffusion limitations of multicomponent mass transport in the electrolyte

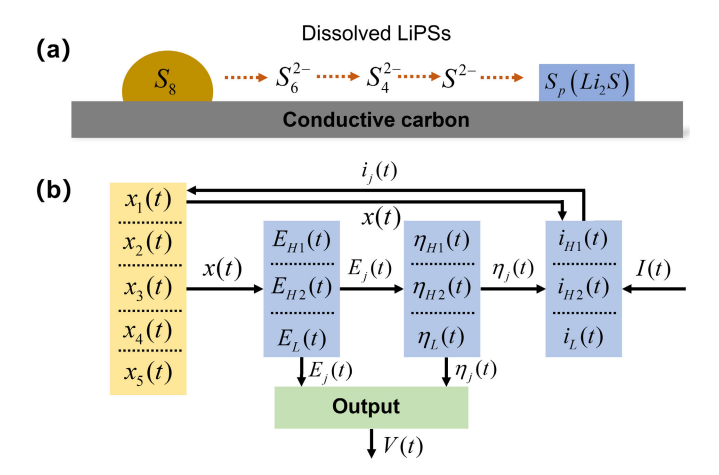


Fig. 2. (a) Schematic of the total reaction pathway during discharge. (b) Block diagram of 0-D model.

have been ignored, which still enables reasonably accurate discharge predictions compared to 1-D models [28]. The symbol  $S^{2-}$   $\downarrow$  represents the precipitation of liquid phase  $S^{2-}$  into solid  $S_p$  in the low plateau, which is modeled by both the precipitation rate  $(k_p)$  and the saturation mass of  $S_p$  in the electrolyte  $(S_s^{2-})$ . These two precipitation-related parameters determine the voltage dip and the low plateau. In this work, we also consider the "shuttle effect," which has not been included in [29]. It is represented by the shuttle constant  $(k_s)$ , which affects the mass evolution of soluble polysulfide species in the high plateau. The dissolved sulfur reacted at anode is neglected, meaning that no loss of total sulfur mass occurs due to the "shuttle effect."

The mass evolution of sulfur species in the 0-D model in Fig. 2(b) is described by the following dynamics:

$$\dot{x}_1 = -\frac{3}{8} \frac{n_{S8} M_S}{n_o F} i_{H1} - k_s x_1 \tag{4}$$

$$\dot{x}_2 = \frac{1}{2} \frac{n_{S6} M_S}{n_e F} i_{H1} + k_s x_1 - k_s x_2 - \frac{n_{S6} M_S}{n_e F} i_{H2}$$
 (5)

$$\dot{x}_3 = \frac{3}{2} \frac{n_{S4} M_S}{n_o F} i_{H2} + k_s x_2 - \frac{1}{6} \frac{n_{S4} M_S}{n_o F} i_L \tag{6}$$

$$\dot{x}_4 = \frac{2}{3} \frac{n_S M_S}{n_e F} i_L - k_p x_5 \left( x_4 - S_*^{2-} \right) \tag{7}$$

$$\dot{x}_5 = k_p x_5 (x_4 - S_*^{2-}) \tag{8}$$

where  $x_1, x_2, x_3, x_4$ , and  $x_5$  denote the mass of sulfur species  $S_8, S_6^{2-}, S_4^{2-}, S^{2-}$ , and  $S_p$ , respectively. The mass evolution of sulfur species in each reaction is governed by the related reaction currents, together with the effect of shuttling and precipitation. The term  $k_s x_i$  in dynamics (4)–(6) represents the effect of shuttling on mass evolution of high-order polysulfides and the precipitation is modeled by a precipitation rate  $k_p$  in dynamics (7) and (8). The model parameters are enumerated in Table I. Next, Nernst equations are used to calculate the equilibrium potentials for reactions (1)–(3) according to

$$E_{H1} = E_{H1}^{0} - \frac{\text{RT}}{F} \left( -\frac{3}{8} \ln \left( \frac{x_1}{n_S M_S v} \right) + \frac{1}{2} \ln \left( \frac{x_2}{n_{S6} M_S v} \right) \right)$$
(9)

TABLE I
0-D MODEL PARAMETERS

Notation	Name	Units
$M_{ m S}$	Molar mass of S	[g/mol]
$n_{\mathrm{S8}}, n_{\mathrm{S6}}, n_{\mathrm{S4}}, n_{\mathrm{S}}$	Number of S atoms in polysulfide	[-]
$n_e$	Number of electron per reaction	[-]
F	Faraday's constant	[C/mol]
R	Gas constant	[J/K/mol]
T	Temperature	[K]
$k_s$	Shuttle constant	$[s^{-1}]$
$k_p$	Precipitation rate	$[s^{-1}]$
$S_*^{2-}$	$S^{2-}$ Saturation mass	[g]
$E_{H1}^0$	Standard potential for reaction 1	[V]
$E_{H2}^0$	Standard potential for reaction 2	[V]
$E_{H2}^{0} \\ E_{L}^{0} \\ i_{H1}^{0}$	Standard potential for reaction 3	[V]
$i_{H1}^0$	Exchange current density for reaction 1	$[A/m^2]$
$i_{H2}^{H1}$	Exchange current density for reaction 2	$[A/m^2]$
$\imath_{L,0}$	Exchange current density for reaction 3	$[A/m^2]$
$\overset{x_{j}^{0}}{\overset{I}{I}}$	Initial mass of species $j$	[g]
${I}$	Applied current	[A]
$a_r$	Active reaction area	$[m^2]$
$a_r^0$	Initial active reaction area	$[m^2]$
$\gamma$	Power of the relative porosity	[-]
$\omega$	Relative porosity change rate constant	[1/g]
v	Electrolyte volume per cell	[L]
$\eta_{H1}, \eta_{H2}, \eta_L$	Surface overpotentials	[V]

$$E_{H2} = E_{H2}^{0} - \frac{\text{RT}}{F} \left( -\ln \left( \frac{x_{2}}{n_{S6}M_{S}v} \right) + \frac{3}{2} \ln \left( \frac{x_{3}}{n_{S4}M_{S}v} \right) \right)$$

$$E_{L} = E_{L}^{0} - \frac{\text{RT}}{F} \left( -\frac{1}{6} \ln \left( \frac{x_{3}}{n_{S4}M_{S}v} \right) + \frac{2}{3} \ln \left( \frac{x_{4}}{n_{S}M_{S}v} \right) \right).$$
(11)

The reaction currents in the three-step electrochemical reactions (1)–(3) are described by Butler–Volmer equations

$$i_{H1} = -i_{H1}^{0} a_{r}$$

$$\cdot \left[ \left( \frac{x_{1}}{x_{1}^{0}} \right)^{-\frac{3}{8}} \left( \frac{x_{2}}{x_{2}^{0}} \right)^{\frac{1}{2}} e^{\frac{F\eta_{H1}}{2RT}} - \left( \frac{x_{1}}{x_{1}^{0}} \right)^{\frac{3}{8}} \left( \frac{x_{2}}{x_{2}^{0}} \right)^{-\frac{1}{2}} e^{-\frac{F\eta_{H1}}{2RT}} \right]$$

$$(12)$$

$$i_{H2} = -i_{H2}^{0} a_{r} \cdot \left[ \left( \frac{x_{2}}{x_{2}^{0}} \right)^{-1} \left( \frac{x_{3}}{x_{3}^{0}} \right)^{\frac{3}{2}} e^{\frac{F\eta_{H2}}{2RT}} - \left( \frac{x_{2}}{x_{2}^{0}} \right) \left( \frac{x_{3}}{x_{3}^{0}} \right)^{-\frac{3}{2}} e^{-\frac{F\eta_{H2}}{2RT}} \right]$$
(13)

$$i_{L} = -i_{L}^{0} a_{r} \cdot \left[ \left( \frac{x_{3}}{x_{3}^{0}} \right)^{-\frac{1}{6}} \left( \frac{x_{4}}{x_{4}^{0}} \right)^{\frac{2}{3}} e^{\frac{F\eta_{L}}{2RT}} - \left( \frac{x_{3}}{x_{3}^{0}} \right)^{\frac{1}{6}} \left( \frac{x_{4}}{x_{4}^{0}} \right)^{-\frac{2}{3}} e^{-\frac{F\eta_{L}}{2RT}} \right].$$

$$(14)$$

The effect of the active reaction area  $a_r$  on the reaction currents is also considered. It is directly related to the precipitate according to

$$a_r = a_r^0 (1 - \omega \cdot x_5)^{\gamma}. \tag{15}$$

The driving force for a reaction to occur at the cathode side is the surface overpotential, which is obtained by the difference between the Nernst potential and the voltage of the cell (V)

$$\eta_{H1} = V - E_{H1} \tag{16}$$

$$\eta_{H2} = V - E_{H2} \tag{17}$$

$$\eta_L = V - E_L. \tag{18}$$

The cell voltage is the measurable output of the system, written compactly as

$$y(t) = h(x(t), z(t)) \tag{19}$$

where the nonlinear output function  $h: \mathbb{R}^5 \times \mathbb{R}^3 \to \mathbb{R}^3$  takes the form

$$h(x,z) = \begin{bmatrix} E_{H1}^{0} - \frac{RT}{F} \left( -\frac{3}{8} \ln \left( \frac{x_{1}}{n_{S8}M_{S8}v} \right) + \frac{1}{2} \ln \left( \frac{x_{2}}{n_{S6}M_{S8}v} \right) \right) + \eta_{H1} \\ E_{H2}^{0} - \frac{RT}{F} \left( -\ln \left( \frac{x_{2}}{n_{S6}M_{S8}v} \right) + \frac{3}{2} \ln \left( \frac{x_{3}}{n_{S4}M_{S8}v} \right) \right) + \eta_{H2} \\ E_{L}^{0} - \frac{RT}{F} \left( -\frac{1}{6} \ln \left( \frac{x_{3}}{n_{S4}M_{S8}v} \right) + \frac{2}{3} \ln \left( \frac{x_{4}}{n_{S}M_{S8}v} \right) \right) + \eta_{L} \end{bmatrix}$$
(20)

The output vector  $y(t) = [y_1(t) \quad y_2(t) \quad y_3(t)]^{\top}$  provides the measured output voltage of Li–S batteries produced from the high and low voltage plateau

$$y_1(t) = \eta_{H1}(t) + E_{H1}(t) \tag{21}$$

$$y_2(t) = \eta_{H2}(t) + E_{H2}(t) \tag{22}$$

$$y_3(t) = \eta_L(t) + E_L(t)$$
 (23)

and  $y_1(t) = y_2(t) = y_2(t) = V(t)$ , which are (equivalent) measured signals.

Finally, the measured cell current *I* is described by the summation of three reaction currents according to charge conservation, i.e.,

$$I = i_{H1} + i_{H2} + i_L. (24)$$

Remark 1: The thermal effects are also critical to battery performance and play a critical role in the dynamics of sulfur evolution. However, due to lack of experimental data and advanced characterization techniques to study the thermal dynamics of Li–S cells, it is challenging to properly integrate and validate a proper temperature model. This aspect will be considered in future works.

# B. Conservation of Sulfur

A critical mathematical property of the model is that sulfur mass is neither created nor destroyed, due to incorrect modeling. We refer to this property as conservation of sulfur mass. Mathematically

$$\frac{d}{dt}m_S(t) = 0, \ m_S(t) = x_1(t) + x_2(t) + x_3(t) + x_4(t) + x_5(t).$$
(25)

It is straightforward to verify the conservation of sulfur mass equation above by substituting the dynamics (4)–(8).

#### C. Equilibrium Analysis

In this section, we analyze the equilibrium structure of the 0-D EM without the shuttle effect. To start, we specify the assumptions used in this equilibrium analysis.

- 1) No shuttle effect:  $k_s = 0$ .
- 2) Zero current:  $i_{H1} = i_{H2} = i_L = I = 0$ .
- 3) Steady-state conditions:  $\dot{x}_i = 0$ , for i = 1, 2, 3, 4, and 5 in (4)–(8).
- 4) The equilibrium voltage  $V^{eq}$  is known.
- 5) The total mass of sulfur species  $m_S$  is known.

Then, the state equilibrium  $(x_1^{\text{eq}}, x_2^{\text{eq}}, x_3^{\text{eq}}, x_4^{\text{eq}}, x_5^{\text{eq}})$  satisfies the following set of equations:

$$V^{\text{eq}} = E_{H1}^{0} - \frac{\text{RT}}{F} \left( -\frac{3}{8} \ln \left( \frac{x_{1}^{\text{eq}}}{n_{S} M_{S} v} \right) + \frac{1}{2} \ln \left( \frac{x_{2}^{\text{eq}}}{n_{S} 6 M_{S} v} \right) \right)$$

$$V^{\text{eq}} = E_{H2}^{0} - \frac{\text{RT}}{F} \left( -\ln \left( \frac{x_{2}^{\text{eq}}}{n_{S} 6 M_{S} v} \right) + \frac{3}{2} \ln \left( \frac{x_{3}^{\text{eq}}}{n_{S4} M_{S} v} \right) \right)$$

$$V^{\text{eq}} = E_{L}^{0} - \frac{\text{RT}}{F} \left( -\frac{1}{6} \ln \left( \frac{x_{3}^{\text{eq}}}{n_{S4} M_{S} v} \right) + \frac{2}{3} \ln \left( \frac{x_{4}^{\text{eq}}}{n_{S} M_{S} v} \right) \right)$$

$$(28)$$

$$m_S = x_1^{\text{eq}} + x_2^{\text{eq}} + x_3^{\text{eq}} + x_4^{\text{eq}} + x_5^{\text{eq}}$$
 (29)

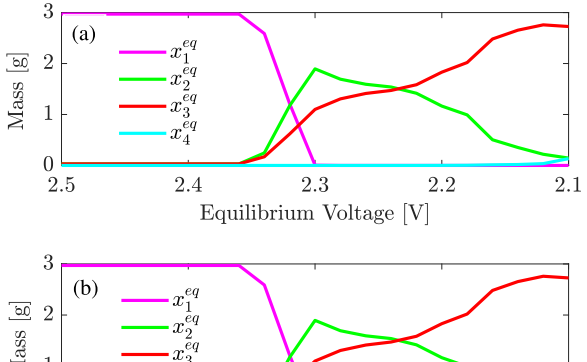
$$0 = x_5^{\text{eq}} \left( x_4^{\text{eq}} - S_*^{2-} \right). \tag{30}$$

Notice that (26)-(30) comprise five equations and five unknowns-the equilibrium states. Since this system of equations is nonlinear, a unique solution is not guaranteed. This contrasts with many electrochemical Li-ion battery models (e.g., SPM) and even ECMs of Li-S cells. Namely, there is no analog to an "OCV" function, which serves as a bijective mapping between the internal states (i.e., element concentrations or masses) and voltage at equilibrium. Nevertheless, two cases for the solutions exist. From (30), we can derive two possible solutions:  $x_5^{\rm eq}=0$  or  $x_4^{\rm eq}=S_*^{2-}$ . We detail both the

- 1) Equilibrium Without Precipitate:  $x_5^{eq} = 0$ . Fig. 3(a) visualizes the equilibrium state values as a function of the equilibrium voltage  $V^{eq}$ .
- 2) Equilibrium With Precipitate:  $x_4^{\text{eq}} = S_*^{2-}$ . Fig. 3(b) visualizes the equilibrium state values as a function of the equilibrium voltage  $V^{eq}$ .

# D. SOC Definition

SOC represents the available discharge capacity in a battery. It is commonly defined as the ratio of the remaining capacity to its maximum capacity [35]. For Li-S batteries, the available capacity is determined by the mass evolution of active sulfur species during battery discharge. Unlike Li-ion batteries, where the SOC can be calculated by the average Li concentration in the solid phase of the negative electrode, it is challenging to define SOC based on polysulfide species in Li-S cells. The multiple reduction reactions with different sulfur species during discharge may lead to multiple SOC definitions associated with different sets of sulfur species. Here, we propose a mathematical SOC definition by considering multiple sulfur



1 2.5 2.4 2.3 2.2 2.1 Equilibrium Voltage [V]

Fig. 3. State equilibria as a function of voltage  $V^{eq}$ . (a) Equilibrium without precipitate. (b) Equilibrium with precipitate.

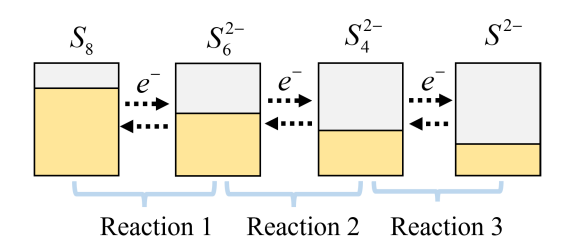


Fig. 4. Mass evolution of reaction products in each reaction and the involved electron transfer.

species, which reflects the "shuttle effect" and the related selfdischarge behavior. As shown in Fig. 4, the reactions (1)–(3)occur simultaneously during discharge. The moles of electrons consumed to produce the sulfur products in each reaction  $(S_6^{2-},$  $S_4^{2-}$ , and  $S^{2-}$ ) are first calculated. Then, this is used to calculate the released capacity, in ampere-hours, of each reaction

$$C_{H1}(t) = \frac{8}{3} \frac{x_1^{100} - x_1(t)}{n_{S8} M_S} \frac{F}{3600}$$

$$C_{H2}(t) = \frac{3}{2} \left[ \frac{x_4(t) - x_4^{100}}{n_S M_S} + \frac{x_5(t) - x_5^{100}}{n_S M_S} \right] \frac{F}{3600}$$
(32)

$$C_{H2}(t) = \frac{3}{2} \left[ \frac{x_4(t) - x_4^{100}}{n_S M_S} + \frac{x_5(t) - x_5^{100}}{n_S M_S} \right] \frac{F}{3600}$$
 (32)

$$C_L(t) = \frac{2}{3} \left[ \frac{x_3(t) - x_3^{100}}{n_{S4} M_S} + \frac{x_4(t) - x_4^{100} + x_5(t) - x_5^{100}}{4 \cdot n_S M_S} \right] \times \frac{F}{3600}$$
(33)

where  $C_{H1}$ ,  $C_{H2}$ , and  $C_L$  are the capacity released in each reaction,  $x_i^{100}$  is the mass of sulfur species i at 100% SOC, and the factor 3600 is used to convert from coulombs to ampere-hours. The total released capacity at time step t can be obtained as

$$C_t(t) = C_{H1}(t) + C_{H2}(t) + C_L(t).$$
 (34)

The SOC definition can then be given by

$$SOC(t) = 1 - \frac{C_t(t)}{C_{\text{max}}}$$
 (35)

where  $C_{\text{max}}$  is the maximum capacity in the cell. Based on this definition, we derive a differential equation governing the evolution of SOC(t)

$$SOC(t) = \frac{-1}{3600 \cdot C_{\text{max}}} \left[ I(t) + \frac{Fk_s}{M_S} \left( \frac{1}{3} x_1(t) + \frac{1}{6} x_2(t) \right) \right].$$
(36)

This equation provides several important insights. First, in the absence of the shuttle effect (i.e.,  $k_s = 0$ ), our SOC definition reduces to Coulomb counting. In the presence of the shuttle effect (i.e.,  $k_s > 0$ ), SOC dissipates in proportion to the masses of  $S_8^0$  and  $S_6^{2-}$ —a property that is distinctly different than Li-ion cells. The factors of (1/3) and (1/6) arise from the stochiometric ratios of sulfur atoms in  $S_8^0$  and  $S_6^{2-}$  to electrons in reactions (1) and (2), respectively.

Remark 2: Although this work focuses on the discharge behaviors of Li–S cells, the same strategy can be used to define the SOC during charging. Since the three-step electrochemical reaction chain (1)–(3) is reversible, the total released capacity of each reaction during charging can be calculated based on the reaction products  $S_4^{2-}$ ,  $S_6^{2-}$ , and  $S_8^{0}$ , which is slightly different than that of the discharging process.

## E. 0-D Li-S Model as a Differential-Algebraic System

To facilitate the subsequent model analysis and state observer designs, a nonlinear differential-algebraic system can be formulated by arranging the nonlinear dynamic equations (4)–(8) and the nonlinear algebraic constraints (9)–(24) into the following compact state-space form:

$$\dot{x}(t) = f(x(t), z(t)) \tag{37}$$

$$0 = g(x(t), z(t), u(t))$$
(38)

$$v(t) = h(x(t), z(t)) \tag{39}$$

where  $x = [x_1 \ x_2 \ x_3 \ x_4 \ x_5]^{\top} \in \mathbb{R}^{n_x}$  with  $n_x = 5$  is the differential state vector representing the mass of sulfur species for  $S_8^0$ ,  $S_6^{2-}$ ,  $S_4^{2-}$ ,  $S^{2-}$ , and  $S_p$ , and  $z = [i_{H1} \ i_{H2} \ i_L]^{\top} \in \mathbb{R}^{n_z}$  with  $n_z = 3$  is the algebraic state vector corresponding to the currents related to the three reactions (1)–(3). Function  $g: \mathbb{R}^5 \times \mathbb{R}^3 \times \mathbb{R} \to \mathbb{R}^3$  is given by

$$g(x(t), z(t), u(t)) = \begin{bmatrix} M_1 z - I \\ M_2 y \end{bmatrix}$$
 (40)

where  $M_1 = \mathbf{1}_{1\times 3}$  is a row vector of ones with three components and

$$M_2 = \begin{bmatrix} 1 & 0 & -1 \\ 0 & 1 & -1 \end{bmatrix}. \tag{41}$$

In particular, (40) is obtained by substitution of (9)–(14) into (16)–(18). The 0-D model (37)–(39) can be conveniently verified to be a semiexplicit DAE of index 1 as  $\partial g/\partial z$  has full rank (invertible) [36]. Typically, a DAE system can be analytically reduced to an ODE system if the function g is linear in z [37]. However, in our case, the function g is highly nonlinear in both z and x, which indicates that it is not straightforward nor necessarily possible to obtain a closed-form solution of constraint (38). Moreover, the original DAE system cannot be fully represented from the reduced-order ODE system and the physical significance of the differential-algebraic states will be suppressed after model reduction [38]. Therefore,

we will conduct all analysis and observer designs based on this nonlinear DAE system without model reductions.

#### III. OBSERVABILITY ANALYSIS

An observability analysis is performed on this DAE system to evaluate whether the differential and algebraic states can be uniquely determined from measurements of input and output signals. In our study, if the nonlinear DAE system is not observable, this means that it is not possible to estimate some internal states from the measurements of current and voltage data. In this section, the local observability of the nonlinear DAE system (37)–(39) is mathematically studied by linearizing the nonlinear DAE system around an equilibrium state, which differs from that of the reformulated ODE system in [29]. The proposed observability analysis can ensure to examine whether both differential and algebraic states are observable.

Let  $w = [x \ z]^{\top} \in \mathbb{R}^{n_w}$ ,  $n_w = n_x + n_z$ , be the augmented state vector. The nonlinear DAE system (37)–(39) is first linearized with a first-order Taylor series expansion around an equilibrium point  $w = w_0$ , which results in a regular linear DAE system

$$E\dot{w}(t) = Aw(t) + Bu(t) \tag{42}$$

$$y = Cw(t). (43)$$

The matrix E is a singular matrix of the form

$$E = \begin{bmatrix} \mathbf{I}_{n_x \times n_x} & \mathbf{0}_{n_x \times n_z} \\ \mathbf{0}_{n_z \times n_x} & \mathbf{0}_{n_z \times n_z} \end{bmatrix}$$
(44)

where **I** is the identity matrix. The state matrix  $A \in \mathbb{R}^{n_w \times n_w}$  and the output matrix  $C \in \mathbb{R}^{3 \times n_w}$  are expressed by

$$A = \begin{bmatrix} \frac{\partial f}{\partial x} & \frac{\partial f}{\partial z} \\ \frac{\partial g}{\partial x} & \frac{\partial g}{\partial z} \end{bmatrix}_{w=w_0} \qquad C = \begin{bmatrix} \frac{\partial h}{\partial x} & \frac{\partial h}{\partial z} \end{bmatrix}_{w=w_0}.$$

The observability conditions are then derived from the linearized system. If the linearized system is observable at an equilibrium point  $w = w_0$ , the nonlinear system is locally observable. Note that the observability results are only sufficient. No conclusions can be obtained for the original nonlinear system if the linearized system is not observable [37].

Here, we apply complete observability (C-observability) to examine whether both differential and algebraic states are observable. The whole state of the system can be uniquely determined by the system output measurements if the system is C-observable. The C-observability for a linear DAE system can be defined as follows.

Theorem 1 (C-Observability [39]): The regular linear DAE system (42) and (43) is completely observable if and only if the following two conditions hold.

C1: 
$$\operatorname{rank}\{[E^{\top}, C^{\top}]^{\top}\} = n_w$$
.  
C2:  $\operatorname{rank}\{[(sE - A)^{\top}, C^{\top}]^{\top}\} = n_w \ \forall s \in \mathbb{C}$ .

The linear system (42) and (43) is C-observable if and only if both the algebraic subsystem (fast subsystem) and the dynamic subsystem (slow subsystem) are observable. The C-observability of the fast subsystem is checked by

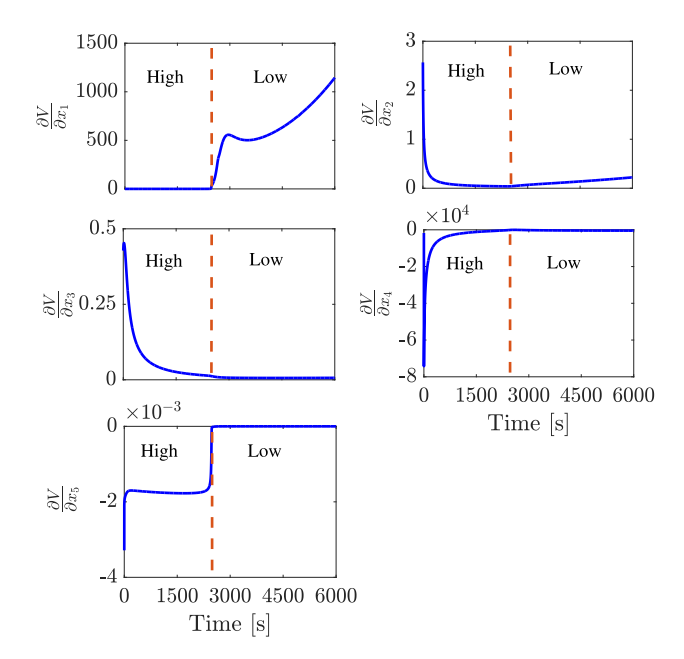


Fig. 5. Sensitivity of output voltage to system states with a constant discharge current at 1 A.

Condition C1, while the C-observability of the fast subsystem is verified by Condition C2. A column rank of  $n_x$  has already been provided by the singular matrix E. It is easy to check Condition C1 whether  $\partial h/\partial z$  has column rank  $n_z$  from (20). Condition C2 needs to be verified through numerical computation of the generalized eigenvalues of the pair (E, A). Although condition C2 has to be validated against all s in a complex domain, it is automatically verified when s is not one of the generalized eigenvalues of pair (E, A).

Although the DAE satisfies the conditions of C-observability, we still do not know if the system is weakly or strongly observable. In this regard, Fig. 5 shows the sensitivity of the system voltage with respect to the dynamic states. The parameter values for simulation are adopted from [28] and [33] and the model was simulated using a constant discharge rate at 1 A. As shown in Fig. 5, the sensitivity for  $x_1$  starts to increase after 2500 s, while the sensitivities for  $x_2$ – $x_5$  vanish after 3000 s, corresponding to the low plateau region, which indicates relatively weak observability in this region. This is a crucial property that we will demonstrate in the numerical studies in Section VI.

Remark 3: Besides C-observability, there exist other forms of observability. For instance, impulse observability (I-observability) reflects the reconstruction ability of the impulse behavior, and R-observability guarantees the observability of any reachable states from the output measurement. Notably, the regular linear DAE system is I-observable or R-observable if it is C-observable [39]. One can choose to verify I/R-observability, but C-observability is more comprehensive and can infer the information of both I-observability and R-observability.

#### IV. MODEL PARAMETERIZATION

In this section, the experimental battery tests are first introduced, followed by the parameter identification of the

three-step 0-D EM using the obtained experimental data. The results of model validation are then presented to demonstrate the accuracy of this 0-D EM.

# A. Experimental Design

Experiments for parameter identification were conducted using a coin cell configuration. The sulfur cathode was fabricated by mixing S@tungsten disulfide/graphene (S@WS<sub>2</sub>/G), conductive agent [multiwall carbon nanotubes (CNTs)], and polymer binder [polyvinylidene fluoride (PVDF)] in a weight ratio of 8:1:1. The mass loading of active S in the cathode was 0.986 mg. Lithium metal foil was used as an anode material and a Celgard 2500 was used as a separator. The electrolyte used was lithiumbis (trifluoromethane sulfonimide) (LiTFSI: 1 M) in a 1,3 dioxolane/1,2-dimethoxyethane (DOL/DME) [1:1 (v/v)] containing 2 wt% lithium nitrate (LiNO<sub>3</sub>) additive. The cell was then tested in a voltage range of 1.7–2.8 V at a discharge current of 1.651 mA (1C) using a land battery test system (CT2001A).

### B. Parameter Identification

Prior to parameter identification, the relative variables and parameters of the 0-D EM are scaled to match the physical sizing of the Li–S coin cell using similitude, as done in [33]. For the 0-D EM, the model parameters to be identified and optimized are

$$\theta = \left[ E_{H1}^{0}, E_{H2}^{0}, E_{L}^{0}, i_{H1}^{0}, i_{H2}^{0}, i_{L}^{0}, k_{s}, k_{p}, \gamma, \omega, m_{S} \right]^{\mathsf{T}}$$
 (45)

where  $E_{H1}$ ,  $E_{H2}$ , and  $E_L$  are the standard potentials,  $i_{H1}$ ,  $i_{H2}$ , and  $i_L$  are the exchanged current density,  $k_s$  is the shuttle rate constant, and  $k_p$ ,  $\gamma$ , and  $\omega$  are the precipitation-related parameters. Finally,  $m_s$  is the total mass of dissolved sulfur in (25). These parameters have been proved to be highly sensitive and largely impact the discharge voltage behavior, even in the weakly observable low plateau region [33]. The objective function for fitting the parameters is expressed as

$$R(k) = \sqrt{\frac{1}{N} \sum_{k=1}^{N} (V_e(k) - V_m(k))^2}$$
 (46)

where R(k) is the root-mean-square error (RMSE) and  $V_e(k)$  and  $V_m(k)$  are the measured experimental voltage and the simulated model voltage at each time step k, respectively. Therefore, the goal is to minimize the objective function (46) with respect to the parameter vector. We applied particle swarm optimization (PSO), an offline gradient-free optimization technique [40].

The identified parameter values are enumerated in Table II. Fig. 6 presents the fitting performance of the three-step 0-D model against the experimental data used for parameter optimization. The simulated voltage matches the measured voltage dynamics well with an RMSE value of 6.44 mV, especially the slope between the high and low plateaus. This is achieved by the additional reaction in the high plateau  $(S_6^{2-} \leftrightarrow S_4^{2-})$ . Then, the model is further validated using experimental data obtained from a cell with another type of cathode material (CNT@S). Fig. 7 shows the comparison of

TABLE II
IDENTIFIED PARAMETER VALUES

Parameters	Values	Units
$E_{H1}^{0}$	2.32	[V]
$E_{H2}^{0}$	2.29	[V]
$\hat{E_L^0}$	2.12	[V]
$i_{H_1}^{0^{2}}$	10	$[A/m^2]$
$i_{H2}^{0^{-1}}$	2	$[A/m^2]$
$i_{L,0}^{112}$	0.02	$[A/m^2]$
$k_s$	1530	$[s^{-1}]$
$k_p$	400	$[s^{-1}]$
$\gamma$	2.5	[-]
$\omega$	1.5	[-]
$m_S$	0.65	[g]

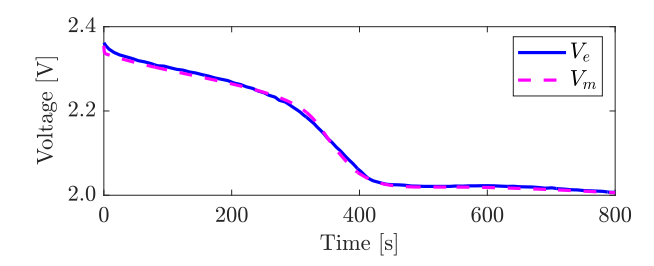


Fig. 6. Fitting performance of 0-D model against the experimental data.

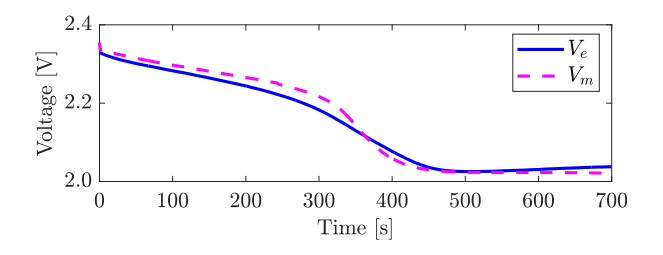


Fig. 7. Validation of the identified 0-D model against experimental data.

the experimentally measured voltage and the model output voltage with the identified parameters during the discharge process. Although the RMSE value increased to 17.22 mV, the simulated voltage can still capture the essential characteristics of the experimental voltage curve.

## V. STATE OBSERVER DESIGN

In this section, an EKF approach for nonlinear DAE systems, similar to the algorithm reported in [41], is used for state estimation. This algorithm applies to measured outputs that are functions of both differential and algebraic state variables. The standard EKF algorithm for ODE systems, however, can only be applied when the differential states are decoupled from the algebraic ones. Then, the algebraic states can be computed as implicit solutions to the nonlinear algebraic constraints at each time step.

To enable the implementation of the proposed algorithm for DAE system, we first transform the nonlinear DAE system (37) and (39) into discrete time using a forward Euler's method

$$x(k+1) = f_d(x(k), z(k)) + \mu(k)$$
(47)

$$0 = g_d(x(k), z(k), u(k))$$
(48)

$$y(k) = h_d(x(k), z(k)) + v(k)$$
 (49)

## Algorithm 1 EKF for Nonlinear DAEs

**Inputs:** u(k), y(k),  $k = 1, 2, \cdots$ **Outputs:**  $\hat{x}(k)$ ,  $\hat{z}(k)$ ,  $k = 1, 2, \cdots$ 

• At time step k, the algebraic equations of DAE system are used to propagate the (consistent) algebraic state estimates to satisfy the algebraic constraints:

$$g(\hat{x}(k), \hat{z}(k), u(k)) = 0.$$

• Given the up-to-date estimates  $\hat{x}_k$  and consistent algebraic state estimates  $\hat{z}_k$ , the differential state estimates are propagated forward in time using the nonlinear discrete-time model and corrected through output error injection as

$$\hat{x}(k+1) = \hat{x}(k) + \Delta t \cdot f(\hat{x}(k), \hat{z}(k)) + K(k) (y(k) - h(\hat{x}(k), \hat{z}(k))).$$

• The covariance matrix of the differential state estimation error is computed by

$$P(k+1) = F(k)P(k)F(k)^{\top} + Q - K(k) (H(k)P(k)H(k)^{\top} + R) K(k)^{\top},$$

and the calculation of Kalman gain matrix is given by

$$K(k) = F(k)P(k)H(k)^{\top} \left(H(k)P(k)H(k)^{\top} + R\right)^{-1}$$

where F(k) and H(k) are the linearized state and output equations with respect to the differential state evaluated at  $\hat{x}(k)$ ,

$$F(k) = \frac{\partial f_d}{\partial x}\Big|_{\hat{x}(k)}, \quad H(k) = \frac{\partial h_d}{\partial x}\Big|_{\hat{x}(k)}.$$

where  $f_d(x(k), z(k))$ ,  $g_d(x(k), z(k), u(k))$ , and  $h_d(x(k), z(k))$ are the discrete-time versions of (37)–(39), respectively;  $f_d(x(k), z(k)) = x(k) + \Delta t \cdot f(x(k), z(k))$  with  $\Delta t$  as the sampling time; x(k) and z(k) are the discretized differential and algebraic states at time  $t = k\Delta t$ , respectively; and  $\mu(k)$  and  $\nu(k)$  are the process and the measurement noises with covariance matrices Q and R, respectively. The forward Euler's method has been selected as a simple-toimplement discretization strategy since it generates a relatively simpler mathematical structure than implicit methods, which significantly benefits the subsequent design efforts for state observers. In addition, as index-1 DAEs are in general not stiff, they can be efficiently handled by Euler's methods [42]. The EKF designed for system (47)–(49) is detailed in Algorithm 1. Essentially, algebraic state estimates that are consistent with the DAE are first computed numerically. The differential states at the next time instant are then predicted using both the differential and algebraic states at time k through the propagation in time of the nonlinear state function. Then, the algorithm corrects the states via output error injection. Subsequently, the covariance matrix of the differential states is computed using the linearized ODE model, followed by the calculation of the Kalman gain matrix using the covariance matrix and the state and output matrices from the linearized model.

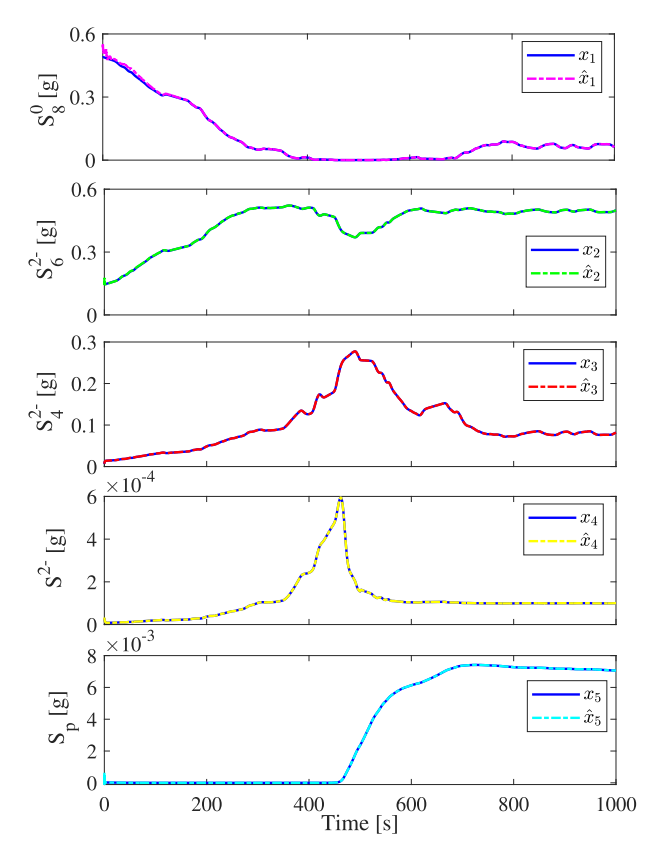


Fig. 8. Comparison of estimated and true mass of sulfur species (i.e., the differential states) under a UDDS cycle with measurement noise.

Note that this algorithm only updates the differential state estimates using the classical Kalman filter approach [43], and the estimated algebraic states are recomputed to satisfy the nonlinear algebraic equations at each time step.

# VI. NUMERICAL RESULTS

In this section, we conduct studies on simulation and experiment to demonstrate the performance of the proposed observer algorithm.

# A. Simulation Results

We first present simulation results that validate the proposed estimation algorithm in Figs. 8 and 9. We consider an urban dynamometer driving schedule (UDDS) drive cycle, which has been frequently used in automotive applications due to its highly dynamic and transient behaviors. It is challenging to experimentally validate the estimation algorithm because no experimental UDDS data for Li-S cell are available at this stage. To address this issue, rather than using experimental UDDS data, we examine the effects of measurement uncertainties to mimic real-world applications by adding a 2% random error to the simulated UDDS voltage signal to validate the robustness of the estimation scheme. To the best of our knowledge, estimation results based on Li-S EM under dynamic driving profiles have not been reported thoroughly in the literature. The current profile is shown in Fig. 9(a) with a maximum C-rate of 3.73C and a mean C-Rate of 0.94C. The parameter values for the plant model and state

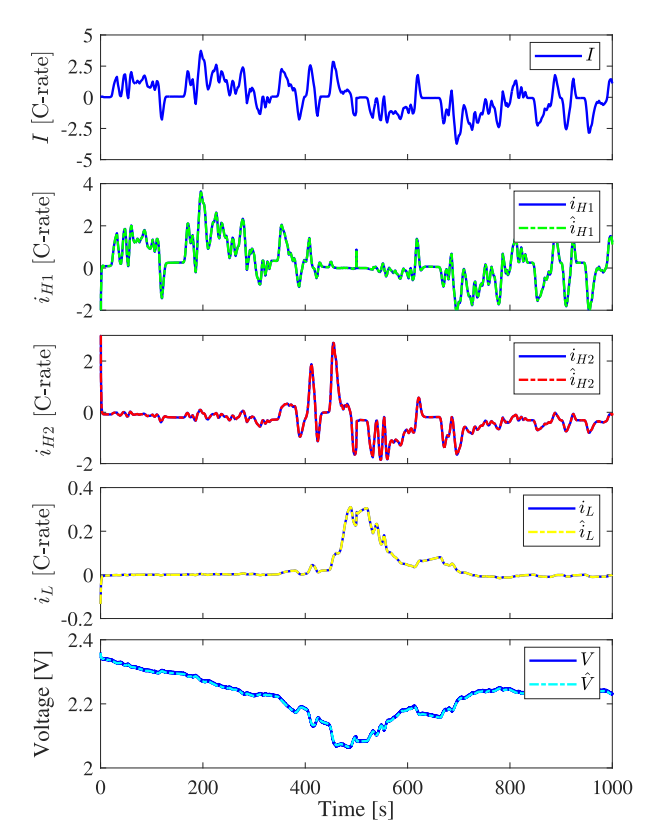


Fig. 9. Comparison of the estimated and true algebraic states ( $i_{H1}$ ,  $i_{H2}$ , and  $i_L$ ) and voltage under a UDDS cycle with measurement noise.

estimator are obtained from [28] and [33]. The observer estimates the differential and algebraic states given the applied current and simulated voltage. The true initial conditions for the internal states are  $w_0 = [0.4875 \quad 0.1560 \quad 0.0065 \quad 3 \times 1e^{-5} \quad 3 \times 1e^{-5} \quad 0.05 \quad 0 \quad 0]^{\top}$ , whereas the observer initial conditions are initialized with an error of 10%. The values of the covariance matrices P(0), Q, and R are set as follows:

$$\begin{split} P(0) &= \mathrm{diag} \big( \big[ 8\mathrm{e}^{-2} & 9.5\mathrm{e}^{-3} & 9\mathrm{e}^{-6} & 5\mathrm{e}^{-6} & 2\mathrm{e}^{-6} \big] \big) \\ Q &= \mathrm{diag} \big( \big[ 5\mathrm{e}^{-14} & 5\mathrm{e}^{-14} & 5\mathrm{e}^{-20} & 5\mathrm{e}^{-23} & 5\mathrm{e}^{-20} \big] \big) \\ R &= \mathrm{diag} \big( \big[ 8\mathrm{e}^{-3} & 1\mathrm{e}^{-5} & 1\mathrm{e}^{-5} \big] \big). \end{split}$$

The estimated mass of each sulfur specie is plotted against their true values in Fig. 8. Fig. 9 shows the estimates for the algebraic states ( $i_{H1}$ ,  $i_{H2}$ , and  $i_L$ ) and the output voltage (V) compared to their true values. The estimates of both the differential and algebraic states quickly converge to their true values. The estimated output voltage is also able to track the simulated voltage accurately. These results demonstrate that the estimated states can still converge to their true values, even with measurement noise, indicating the robustness of our proposed estimation algorithm under a highly dynamic scenario, such as EVs.

## B. Experimental Results

The proposed estimation algorithm is then experimentally validated in this section. The parameter values for both the plant model and estimator are obtained from the parameter

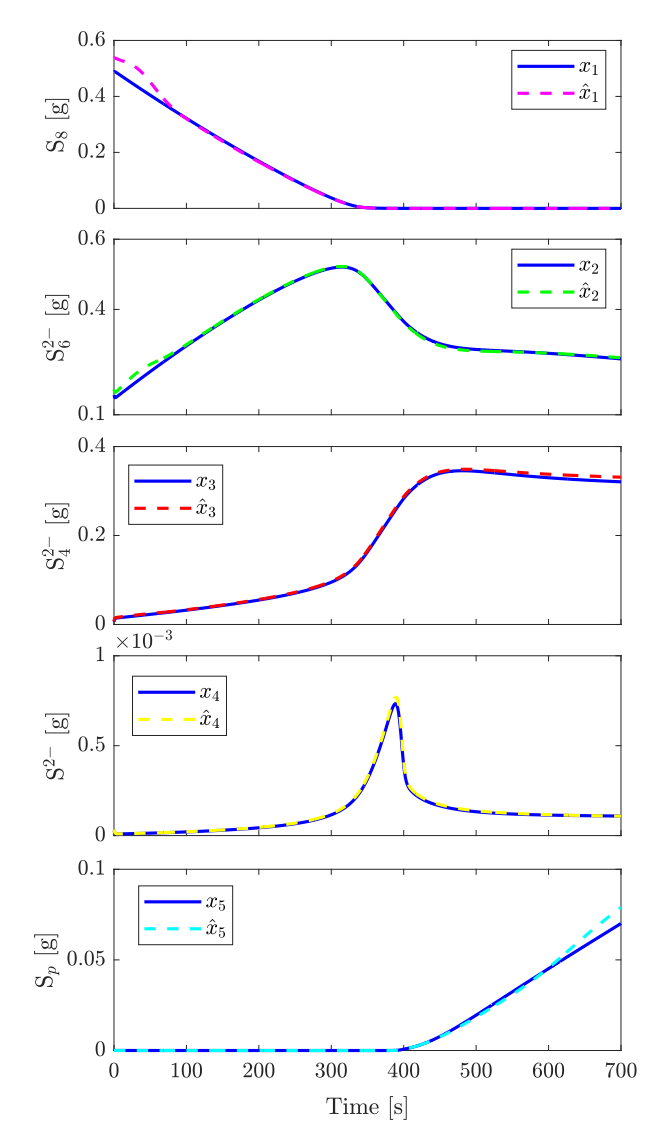


Fig. 10. Comparison of estimated and true mass of sulfur species (i.e., the differential states) under a 1C discharge cycle.

identification results in Section IV. A constant discharge C-rate of 1C that was used in our experiment was applied to the plant model for 700 s. Note that due to the difficulty in verifying in situ the internal states in a real battery, the states simulated from the EM with parameters identified from a real battery were used to emulate the truth values of the internal states. The initial guess error for the state estimates of the observer was set to 10%. These results are generated numerically by tuning the following parameters in the EKF:

$$P(0) = \operatorname{diag}([2.5e^{-8} \quad 2.5e^{-8} \quad 2e^{-11} \quad 2e^{-11} \quad 2e^{-11}])$$

$$Q = \operatorname{diag}([1e^{-10} \quad 1e^{-10} \quad 1e^{-21} \quad 1e^{-25} \quad 1e^{-21}])$$

$$R = \operatorname{diag}([1e^{-5} \quad 1e^{-5} \quad 1e^{-5}]).$$

Fig. 10 reports the state estimation results for the differential states under a constant 1C discharge current, plotted in Fig. 11(a). Fig. 11 further compares the estimated algebraic states and output voltage against their true values. The solid lines denote true values, and the dashed lines denote estimates. Since the battery is discharged from a fully charged state,

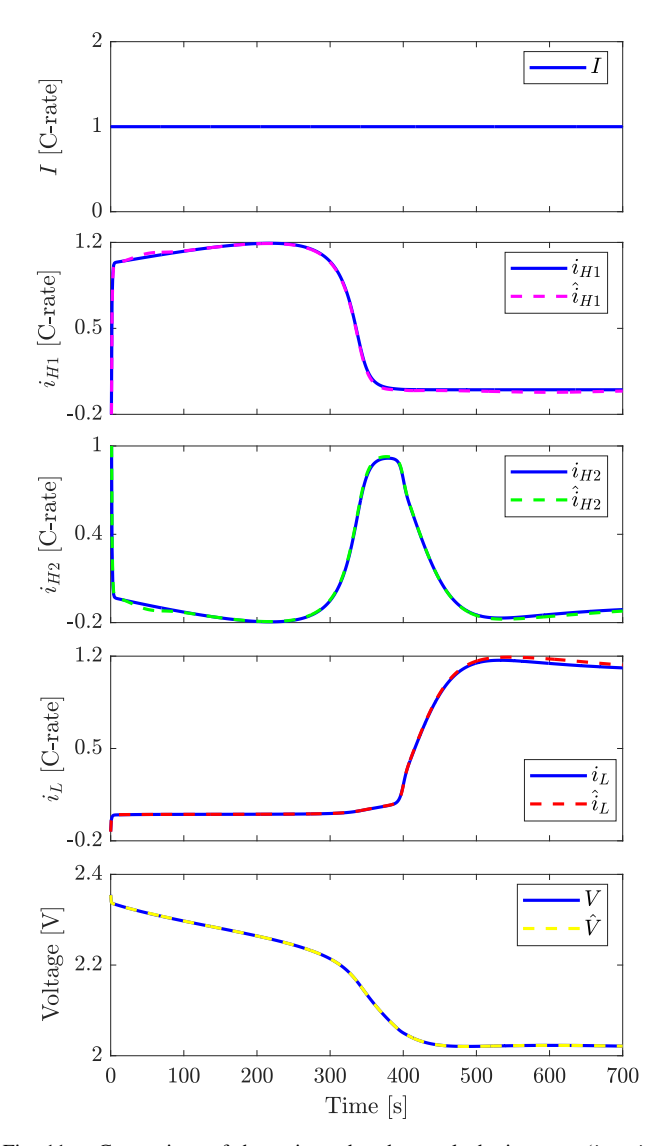


Fig. 11. Comparison of the estimated and true algebraic states  $(i_{H1}, i_{H2},$  and  $i_L)$  and voltage under a 1C discharge cycle.

all state estimates are able to quickly converge to their true values from 10% initial estimation errors within 100 s, due to the high observability in the high plateau (see observability analysis in Fig. 5). However, unsurprisingly, note that the estimates of  $S_4^{2-}$  and  $S_p$  show slight divergence in the low plateau region, which is mainly caused by the weak observability of the Li-S system. To improve the estimation performance in the low observability region, in addition to tuning the EKF-related parameters such as covariance matrices Q, we could potentially explore a hybrid estimation framework. Specifically, two EKFs can be individually designed for high plateau and low plateau coupled with a switching scheme at the intersection of high-to-low regions. Another possible pathway to improve observability is by adding additional sensors to introduce more measurement signals (e.g., temperature, pressure, and strain). These options will be exploited in our future studies.

## C. SOC Simulation Results

Simulation results for the proposed SOC definition are evaluated in this section. Our proposed method is based on the

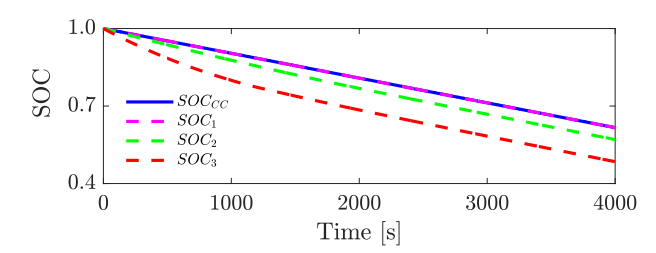


Fig. 12. SOC values calculated by Coulomb counting and the proposed methods considering different shuttle rates.

remaining discharge capacity calculation, which depends on the active sulfur species. We also perform a sensitivity analysis on the "shuttle effect." In Li-S cell, the "shuttle effect" changes the mass evolution behavior of sulfur species by introducing a self-discharge-like process. This affects the remaining discharge capacity and also the related SOC. Fig. 12 presents the simulation results calculated by traditional Coulomb counting and the proposed method with different shuttle rates at a constant 1.7-A discharge current. The SOC calculated by the proposed method in the absence of "shuttle effect" shows no difference with Coulomb counting. However, when the shuttle rate is increased to  $2 \times 10^{-4}$ , the SOC calculated by the proposed method decreases much faster. This trend becomes more pronounced as the shuttle rate increases. That is because the "shuttle effect" is a self-discharge process that does not contribute to the reaction current. Therefore, it results in less remaining discharge capacity. These results demonstrate that our proposed method can represent the effect of shuttling on capacity loss and the subsequent SOC evolution. Note that for Li-ion batteries, the relationship between bulk lithium concentration in the anode and SOC is one-to-one. This means that the bulk lithium concentration can be determined once the SOC is known and vice versa. However, the relationship between sulfur species and SOC becomes complicated in Li-S cells. There are different combinations of sulfur species to SOC if the SOC is known, which means that the relationship between them is not one-to-one.

Remark 4: Despite the capability to represent the shuttling effect on capacity loss and the subsequent SOC evolution accurately, the SOC calculation scheme cannot be validated experimentally due to the difficulty of precisely measuring the mass of sulfur species in real time as a result of the lack of in situ characterization techniques. Nevertheless, data generated from higher dimensional Li–S EMs may be considered as the ground truth for validation, which will be explored in our future works.

### VII. CONCLUSION

In this article, we studied a 0-D EM that shows practical use for estimation and control purposes for next-generation high energy density Li–S batteries. A state estimation algorithm for the developed model has been presented. The observability of this nonlinear DAE system has been investigated, which indicates that the states are locally observable but show weak observability in the low plateau region. The model is identified and experimentally validated using the experimental data collected from Li–S coin cell. An extended Kalman filter-based

algorithm is then adopted to estimate the amount of active sulfur species and the reaction currents in simulation with dynamic current profile. The developed estimation algorithm is further validated using the experimental data. The accuracy of the estimation approach is demonstrated in both simulation and experiment. Moreover, we proposed the SOC definition by different sulfur species, which can well represent the "shuttle effect" and self-discharge behavior.

Future work will focus on examining the robustness of the proposed estimation algorithm against the parameter uncertainties. In addition, reduced-order EM-based SOC and SOH estimation approaches will also be studied.

### REFERENCES

- [1] J. Liu et al., "Pathways for practical high-energy long-cycling lithium metal batteries," *Nature Energy*, vol. 4, no. 3, pp. 180–186, Feb. 2019.
- [2] D. Liu et al., "Catalytic effects in lithium–sulfur batteries: Promoted sulfur transformation and reduced shuttle effect," Adv. Sci., vol. 5, no. 1, Jan. 2018, Art. no. 1700270.
- [3] M. Zhao, B.-Q. Li, X.-Q. Zhang, J.-Q. Huang, and Q. Zhang, "A perspective toward practical lithium–sulfur batteries," ACS Central Sci., vol. 6, no. 7, pp. 1095–1104, 2020.
- [4] C. D. Parke, L. Teo, D. T. Schwartz, and V. R. Subramanian, "Progress on continuum modeling of lithium-sulfur batteries," *Sustain. Energy Fuels*, vol. 5, no. 23, pp. 5946–5966, 2021.
- [5] N. A. Chaturvedi, R. Klein, J. Christensen, J. Ahmed, and A. Kojic, "Algorithms for advanced battery-management systems," *IEEE Control Syst. Mag.*, vol. 30, no. 3, pp. 49–68, Jun. 2010.
- [6] Y. Wang et al., "A comprehensive review of battery modeling and state estimation approaches for advanced battery management systems," *Renew. Sustain. Energy Rev.*, vol. 131, Oct. 2020, Art. no. 110015.
- [7] R. Xiong, J. Cao, Q. Yu, H. He, and F. Sun, "Critical review on the battery state of charge estimation methods for electric vehicles," *IEEE Access*, vol. 6, pp. 1832–1843, 2018.
- [8] Y. V. Mikhaylik and J. R. Akridge, "Polysulfide shuttle study in the Li/S battery system," J. Electrochem. Soc., vol. 151, no. 11, p. A1969, 2004.
- [9] H. S. Ryu, Z. Guo, H. J. Ahn, G. B. Cho, and H. Liu, "Investigation of discharge reaction mechanism of lithium|liquid electrolyte|sulfur battery," *J. Power Sources*, vol. 189, no. 2, pp. 1179–1183, Apr. 2009.
- [10] K. S. Hariharan and V. Senthil Kumar, "A nonlinear equivalent circuit model for lithium ion cells," *J. Power Sources*, vol. 222, pp. 210–217, Jan. 2013.
- [11] D. Zhang, S. Dey, H. E. Perez, and S. J. Moura, "Remaining useful life estimation of lithium-ion batteries based on thermal dynamics," in *Proc. Amer. Control Conf. (ACC)*, May 2017, pp. 4042–4047.
- [12] S. J. Moura, F. B. Argomedo, R. Klein, A. Mirtabatabaei, and M. Krstic, "Battery state estimation for a single particle model with electrolyte dynamics," *IEEE Trans. Control Syst. Technol.*, vol. 25, no. 2, pp. 453–468, Mar. 2017.
- [13] D. Zhang, S. Dey, L. D. Couto, and S. J. Moura, "Battery adaptive observer for a single-particle model with intercalation-induced stress," *IEEE Trans. Control Syst. Technol.*, vol. 28, no. 4, pp. 1363–1377, Jul. 2020.
- [14] R. Klein, N. A. Chaturvedi, J. Christensen, J. Ahmed, R. Findeisen, and A. Kojic, "Electrochemical model based observer design for a lithium-ion battery," *IEEE Trans. Control Syst. Technol.*, vol. 21, no. 2, pp. 289–301, Mar. 2013.
- [15] V. Knap, D.-I. Stroe, R. Teodorescu, M. Swierczynski, and T. Stanciu, "Electrical circuit models for performance modeling of lithium-sulfur batteries," in *Proc. IEEE Energy Convers. Congr. Expo. (ECCE)*, Sep. 2015, pp. 1375–1381.
- [16] K. Propp et al., "Multi-temperature state-dependent equivalent circuit discharge model for lithium-sulfur batteries," *J. Power Sources*, vol. 328, pp. 289–299, Oct. 2016.
- [17] A. Fotouhi et al., "Lithium-sulfur cell equivalent circuit network model parameterization and sensitivity analysis," *IEEE Trans. Veh. Technol.*, vol. 66, no. 9, pp. 7711–7721, Sep. 2017.
- [18] D.-I. Stroe, V. Knap, M. Swierczynski, and E. Schaltz, "Electrochemical impedance spectroscopy-based electric circuit modeling of lithium– sulfur batteries during a discharging state," *IEEE Trans. Ind. Appl.*, vol. 55, no. 1, pp. 631–637, Jan. 2019.

- [19] K. Propp, D. J. Auger, A. Fotouhi, S. Longo, and V. Knap, "Kalman-variant estimators for state of charge in lithium-sulfur batteries," *J. Power Sources*, vol. 343, pp. 254–267, Mar. 2017.
- [20] K. Propp, D. J. Auger, A. Fotouhi, M. Marinescu, V. Knap, and S. Longo, "Improved state of charge estimation for lithium-sulfur batteries," *J. Energy Storage*, vol. 26, Dec. 2019, Art. no. 100943.
- [21] A. Jokar, B. Rajabloo, M. Désilets, and M. Lacroix, "Review of simplified pseudo-two-dimensional models of lithium-ion batteries," *J. Power Sources*, vol. 327, pp. 44–55, Sep. 2016.
- [22] H. E. Perez, S. Dey, X. Hu, and S. J. Moura, "Optimal charging of Li-ion batteries via a single particle model with electrolyte and thermal dynamics," *J. Electrochem. Soc.*, vol. 164, no. 7, pp. 1679–1687, 2017.
- [23] K. Kumaresan, Y. Mikhaylik, and R. E. White, "A mathematical model for a lithium–sulfur cell," *J. Electrochem. Soc.*, vol. 155, no. 8, p. A576, 2008.
- [24] A. F. Hofmann, D. N. Fronczek, and W. G. Bessler, "Mechanistic modeling of polysulfide shuttle and capacity loss in lithium–sulfur batteries," *J. Power Sources*, vol. 259, pp. 300–310, Aug. 2014.
- [25] V. Thangavel et al., "A microstructurally resolved model for Li-S batteries assessing the impact of the cathode design on the discharge performance," J. Electrochem. Soc., vol. 163, no. 13, pp. 2817–2829, 2016.
- [26] N. B. Emerce and D. Eroglu, "Effect of electrolyte-to-sulfur ratio in the cell on the Li-S battery performance," *J. Electrochem. Soc.*, vol. 166, no. 8, pp. 1490–1500, 2019.
- [27] G. Wen et al., "Insights into multiphase reactions during self-discharge of Li-S batteries," *Chem. Mater.*, vol. 32, no. 11, pp. 4518–4526, Jun. 2020.
- [28] M. Marinescu, T. Zhang, and G. J. Offer, "A zero dimensional model of lithium-sulfur batteries during charge and discharge," *Phys. Chem. Chem. Phys.*, vol. 18, no. 1, pp. 584–593, 2016.
- [29] C. Xu et al., "Online state estimation for a physics-based lithium-sulfur battery model," J. Power Sources, vol. 489, Mar. 2021, Art. no. 229495.
- [30] Z. Huang, D. Zhang, L. D. Couto, Q.-H. Yang, and S. J. Moura, "State estimation for a zero-dimensional electrochemical model of lithiumsulfur batteries," in *Proc. Amer. Control Conf. (ACC)*, May 2021, pp. 3114–3119.
- [31] W. Lim, S. Kim, C. Jo, and J. Lee, "A comprehensive review of materials with catalytic effects in Li–S batteries: Enhanced redox kinetics," *Angew. Chem.*, vol. 131, no. 52, pp. 18920–18931, Dec. 2019.
- [32] T. Zhang, M. Marinescu, L. O'Neill, M. Wild, and G. Offer, "Modeling the voltage loss mechanisms in lithium–sulfur cells: The importance of electrolyte resistance and precipitation kinetics," *Phys. Chem. Chem. Phys.*, vol. 17, no. 35, pp. 22581–22586, 2015.
- [33] C. Xu, T. Cleary, G. Li, D. Wang, and H. Fathy, "Parameter identification and sensitivity analysis for zero-dimensional physics-based lithiumsulfur battery models," ASME Lett. Dyn. Syst. Control, vol. 1, no. 4, Oct. 2021, Art. no. 041001.
- [34] D. N. Fronczek and W. G. Bessler, "Insight into lithium-sulfur batteries: Elementary kinetic modeling and impedance simulation," *J. Power Sources*, vol. 244, pp. 183–188, Dec. 2013.
- [35] J. Meng et al., "An overview and comparison of online implementable SOC estimation methods for lithium-ion battery," *IEEE Trans. Ind. Appl.*, vol. 54, no. 2, pp. 1583–1591, Mar. 2018.
- [36] K. E. Brenan, S. L. Campbell, and L. R. Petzold, Numerical Solution of Initial-Value Problems in Differential-Algebraic Equations. Philadelphia, PA, USA: SIAM, 1995.
- [37] D. Zhang, L. D. Couto, S. Benjamin, W. Zeng, D. F. Coutinho, and S. J. Moura, "State of charge estimation of parallel connected battery cells via descriptor system theory," in *Proc. Amer. Control Conf. (ACC)*, Jul. 2020, pp. 2207–2212.
- [38] D. Zhang, L. D. Couto, R. Drummond, S. Sripad, and V. Viswanathan, "Cell-level state of charge estimation for battery packs under minimal sensing," 2021, arXiv:2109.08332.
- [39] G.-R. Duan, *Analysis and Design of Descriptor Linear Systems*, vol. 23. Berlin, Germany: Springer, 2010.
- [40] S. Ebbesen, P. Kiwitz, and L. Guzzella, "A generic particle swarm optimization MATLAB function," in *Proc. Amer. Control Conf. (ACC)*, Jun. 2012, pp. 1519–1524.
- [41] L. D. Couto and M. Kinnaert, "Internal and sensor fault detection and isolation for Li-ion batteries," *IFAC-PapersOnLine*, vol. 51, no. 24, pp. 1431–1438, 2018.
- [42] C. W. Gear and L. R. Petzold, "ODE methods for the solution of differential/algebraic systems," SIAM J. Numer. Anal., vol. 21, no. 4, pp. 716–728, Aug. 1984.

[43] G. Goodwin and K. S. Sin, Adaptive Filtering Prediction and Control. Englewood Cliffs, NJ, USA: Prentice-Hall, 1984.



**Zhijia Huang** received the Ph.D. degree from the Department of Materials Science and Engineering, Tsinghua University, Beijing, China, in 2021.

From 2021 to 2022, he was a Post-Doctoral Researcher with the University of California at Berkeley, Berkeley, CA, USA. His research interests include high-energy-density battery material design, modeling and estimation, and machine learning toward advanced energy storage devices and systems.



Luis D. Couto received the bachelor's degree in chemical engineering from Simón Bolívar University, Caracas, Venezuela, in 2013, the master's degree in renewable energies from the Autonomous University of Madrid, Madrid, Spain, in 2014, and the Ph.D. degree from the Free University of Brussels, Brussels, Belgium, in 2018.

In 2020, he was a Visiting Scholar at the Department of Engineering Science, University of Oxford, Oxford, U.K. In 2022, he was a Post-Doctoral Researcher with the Department of Control Engi-

neering and System Analysis, Free University of Brussels. He is currently a Researcher in electrical energy storage at the Unit Energy Technology, VITO (Flemish Institute for Technological Research), Mol, Belgium. His current research interests include state/parameter estimation, fault diagnosis, and optimal control in the context of battery management systems.



Chitra Dangwal received the bachelor's degree from MNNIT Allahabad, Prayagraj, India, in 2016, and the M.S. degree in mechanical engineering from The Ohio State University, Columbus, OH, USA, in 2020. She is currently pursuing the Ph.D. degree in system engineering from the University of California Berkeley, Berkeley, CA, USA, with a focus on control and estimation problems related to Li-ion batteries.

From 2016 to 2018, she worked as an Engine Calibration Engineer at the Research and Develop-

ment Facility, Bajaj Auto Ltd., Pune, India. Her current work and interest lie in electrochemical modeling, controls, and estimation with application to batteries.



**Shujie Xiao** received the B.S. and Ph.D. degrees from the School of Materials Science and Engineering, Tsinghua University, Beijing, China, in 2022 and 2015, respectively.

He currently works in industry as a Research and Development Engineer, Huayou Cobalt, Tongxiang, Zhejiang, China. His current research interests include commercial cathode materials and advanced cathode materials of lithium-ion (Li-ion) batteries and the corresponding additives.



Wei Lv received the Ph.D. degree in applied chemistry from the School of Chemical Engineering and Technology, Tianjin University, Tianjin, China, in 2012.

He is currently an Associate Professor at the Tsinghua Shenzhen International Graduate School, Tsinghua University, Shenzhen, China. His recent research interests mainly focus on solving the problems of lithium–sulfur (Li–S) batteries by designing and preparing the carbon hosts with precisely tuned structure, and the catalysts promoting the reaction

kinetics of sulfur and stable lithium metal anode.

Dr. Lv also serves as a member of the Youth Editorial Committee for *InfoMat* and *Chinese Chemical Letters*, an Editorial Board Member for *Molecules*, and an Associate Editor for *Frontiers in Materials*.



Dong Zhang received the B.S. degree in civil and environmental engineering from the University of Michigan, Ann Arbor, MI, USA, in 2015, the B.S. degree in electrical and computer engineering from Shanghai Jiao Tong University, Shanghai, China, in 2015, and the M.S. and Ph.D. degrees in systems and control engineering from the University of California at Berkeley, Berkeley, CA, USA, in 2016 and 2020, respectively.

He was a Post-Doctoral Fellow with the Department of Mechanical Engineering, Carnegie Mellon

University, Pittsburgh, PA, USA, from 2020 to 2021. He is currently an Assistant Professor in aerospace and mechanical engineering at The University of Oklahoma, Norman, OK, USA, while directing the Energy Systems and Controls Laboratory. He is also a Faculty Affiliate with the Institute for

Resilient Environmental and Energy Systems (IREES), The University of Oklahoma. His current research interests include dynamical system control, state estimation, optimization, machine learning, energy storage, and advanced lithium-ion battery management systems.

Dr. Zhang was a recipient of the Best Paper Award by the ASME Energy System Technical Committee at the 2020 American Control Conference.



**Scott J. Moura** (Member, IEEE) received the B.S. degree from the University of California at Berkeley (UC Berkeley), Berkeley, CA, USA, in 2006, and the M.S. and Ph.D. degrees from the University of Michigan, Ann Arbor, MI, USA, in 2008 and 2011, respectively.

He was a Post-Doctoral Fellow with the University of California at San Diego, La Jolla, CA, USA, from 2011 to 2013. From 2015 to 2021, he was a Principal Investigator (PI) with the Tsinghua-Berkeley Shenzhen Institute, Shenzhen,

China. In 2013, he was a Visiting Researcher with MINES ParisTech, Paris, France. He is currently the Clare and Hsieh Wen Shen Endowed Distinguished Professor, the Director of the Energy, Control, and Applications Laboratory (eCAL), the PATH Faculty Director, and the Chair of engineering science with UC Berkeley. His research interests include control, optimization, and data science for batteries, electrified vehicles, and climate-tech.

Dr. Moura received the American Society of Mechanical Engineers (ASME) Dynamic Systems and Control Division Young Investigator Award, the National Science Foundation CAREER Award, the Carol D. Soc Distinguished Graduate Student Mentor Award, the O. Hugo Shuck Best Paper Award, the UC Presidential Postdoctoral Fellowship, and the National Science Foundation (NSF) Graduate Research Fellowship.